Permeability Mapping in Naturally Heterogeneous Sandstone Cores by Magnetization Prepared Centric-Scan SPRITE

Konstantin Romanenko and Bruce J. Balcom
MRI Centre, Dept. of Physics, University of New Brunswick, P.O. Box 4400, 8 Bailey Drive, Fredericton, E3B 5A3, Canada

DOI 10.1002/aic.13778
Published online April 10, 2012 in Wiley Online Library (wileyonlinelibrary.com).

A time-efficient MRI method suitable for quantitative two-dimensional (2-D) mapping of permeability in sedimentary rock cores, and granular media samples is discussed. The images of porosity and mean axial velocity in the plane transverse to the average flow direction are essential to determine 2-D distribution of permeability in a core sample. The 2-D permeability mapping is particularly useful for discrimination of bedding and lamination layers, fractures and fault facies that occur in sedimentary rocks. The proposed method combines the 13-interval APGSTE scheme and centric-scan SPRITE. The APGSTE scheme is known to substantially reduce gradient-related errors in diffusion measurements. The SPRITE method provides quantitative information on fluid content within the core samples. The experiment time is critically reduced when only a few samples near the q*-space origin are collected. The APGSTE-SPRITE method is illustrated through mapping of 2-D permeability and 3-D velocity field in naturally heterogeneous sandstone cores.* *AIChE J,* 58: 3916–3926, 2012
Keywords: porous media, petroleum, MRI, rheology

Introduction

The concept of permeability is central for hydrocarbon recovery from petroleum reservoirs and for studies of groundwater flow in aquifers. The heterogeneity of natural formations determines the spreading of solutes in groundwater. Most sedimentary rocks have spatial variations in bedding structure and may contain distinct domains of fixed permeability, and fractures. Predictions of oil recovery are based on well-logging data and laboratory core analysis. Conventional laboratory measurements of absolute permeability are straightforward and based on direct application of the Darcy equation. Measurements of macroscopic flow rate, pressure drop and sample dimensions are required. Although these measurements are precise, the resulting average permeability values may mask valuable information on heterogeneity within the sample. Robust bulk NMR measurements are commonly applied for prediction of pore-size distribution and permeability in nonflowing systems.[1,2] These correlation-based techniques provide rough estimations of physical characteristics averaged over the core sample. Measurements of permeability in sedimentary rocks with spatial resolution and under flow conditions are far more challenging. Techniques potentially useful for multidimensional permeability mapping are rarely discussed in the literature.[3–5] Velocity mapping experiments in model percolation objects using spin-echo MRI were reported by Klemm[6] and Webber and Kimmich.[7] A 1-D mapping approach based on gas-phase MRI was proposed by Bencsik and Ramanathan.[8]

The internal magnetic field gradients in sedimentary rocks can be strong enough to make the spin-echo MRI measurements meaningless. Li et al.[9] proposed a combination of an alternating-pulsed-gradient stimulated-echo (APGSTE) sequence[10,11] with centric-scan SPRITE (single-point ramped imaging with T_1 enhancement) read-out[12,13] for flow velocity imaging. The combined techniques substantially reduce errors due to internal magnetic field gradients. The use of this pulse sequence along with the correct treatment of the spatially resolved velocity distributions allowed quantitative 2-D mapping of mean velocity and permeability in model porous materials.[14] SPRITE is a pure phase encoding imaging technique. It is largely immune to susceptibility contrast induced gradients, paramagnetic impurities, chemical shift and other potential time-evolution effects.[12,13,14–19]

The propagator representation of flow and diffusion[20] yields quantitative information on flow and hydrodynamic dispersion in porous media.[21–24] Measurements of high-quality propagators with spatial resolution are very time-consuming. The key idea for time efficient mapping of the flow is to consider the origin of q-space only. Acquisition of a small number of q-space points takes a relatively short time and provides accurate mean velocity values.

2-D permeability measurement

For viscous nonturbulent flow the linear relationship between the flow rate and the pressure drop is satisfied by Darcy's law

Correspondence concerning this article should be addressed to K. Romanenko at kromanen@unb.ca or B. J. Balcom at bjb@unb.ca.

$$\frac{Q}{s} = \frac{K \cdot \Pi}{L \cdot \mu}, \tag{1}$$

where Q is the total volumetric flow rate, s is the total cross section of the core sample, K is the absolute permeability, Π is the pressure drop, L is the length of the core sample, μ is the dynamic viscosity. Mean velocity over the core sample is given by

$$<V>_{bulk} = \frac{Q}{s \cdot \emptyset} = \frac{K \cdot \Pi}{L \cdot \mu \cdot \emptyset}, \tag{2}$$

where Ø is the average porosity of the sample.

Based on the analogy of Darcy's and Ohm's laws the permeability of the "parallel circuit", K_P, can be expressed as follows

$$K_P = \frac{\sum s_i \cdot K_i}{s}, \tag{3}$$

where s and s_i are total and elementary cross sections of the sample, respectively.

Moving to a description of 2-D imaging of flow one can assign the elements of a porous sample s_i, to pixels of an image. For a parallel connection of N pixels $s_i = s/N$ and Eq. 3 becomes

$$K_P = \frac{\sum K_i}{N} \tag{4}$$

The cumulative flow in the z-direction is a sum of fluxes through the elementary cross sections $\delta x \cdot \delta y$ in the x-y plane. The pressure, Π, drop in the parallel flow system is the same for all its components. The flow rate across each elementary cross section $\delta x \cdot \delta y$ scales proportionally with the total pressure drop since the Darcy's law is valid for each 2-D element of the core

$$\mathrm{K(x,y)} = \frac{\emptyset(x,y) \cdot <V_Z>(x,y) \cdot \mu \cdot L}{\Pi}, \tag{5}$$

where $\emptyset(x,y)$ and $<V_Z>(x,y)$ are 2-D maps of porosity and mean axial velocity, respectively. $<V_Z>(x,y)$ should ideally be an instantaneous average velocity vector. In practice, we assume that the measured macroscopic velocity vector $<V_Z>(x,y)$ is averaged over a short time interval, so that the influence of hydrodynamic dispersion is minimized. The errors of porosity and velocity measurements are described in detail below.

Averaging along the core implies certain limitations on choice of the samples. Ideal samples would be the natural parallel flow systems like layered or fractured sedimentary rocks, and samples with fault facies oriented along the core. Laminations and beds are planar structures that may vary in size from a few hundred microns to many centimeters. These textural features of the rock can be fairly well distinguished with MRI. In the case of layered sedimentary rocks, it would be recommended to examine cores drilled along and across the layers to test the permeability variation in different planes. Different orientations of sedimentary layers with respect to the average flow direction will manifest in different permeability contrasts. Indeed, the 2-D permeability map may not reveal any contrast when layers are oriented at large angles with respect to the core axis.

The permeability map will be uniform when the core sample is homogeneous on a scale greater than the MRI resolution. A quantitative 2-D permeability map satisfies Eq. 4 whether permeability contrast is observed or not. It may be hard to interpret the 2-D permeability contrast in sedimentary rocks, such as carbonates. Carbonates are characterized by different types of porosity and complex pore-size distributions. However, the ability to observe this contrast is a significant advantage over existing NMR permeability correlations. Carbonate sedimentary rocks and sandstones with random texture can be examined with quantitative 3-D imaging of porosity and velocity field.

The simple boundary condition does not apply in 3-D case. Reconstruction of a 3-D permeability map from full velocity field and 3-D porosity requires knowledge of the pressure distribution within the core. Lattice Boltzmann simulations of flow in porous media could provide a solution to this problem.[25]

A number of factors may affect permeability measurements. Potential permeability alteration should be expected from interaction of rock constituents and fluids; confining stress and temperature.[26] Most common mechanisms of formation damage are related to clay swelling, fines mobilization, migration and deposition, phase trapping, wettability alteration, biological activity, etc. It is generally advised to use brine instead of distilled water to avoid clay swelling. Flow velocities on the order of a few millimeters per second are standard for many types of liquid permeability tests. These velocities, however, significantly exceed the values encountered in field conditions (a few feet per day). High-flow rates in laboratory tests can cause permeability alteration due to fines migration.[27]

Porosity mapping with centric-scan SPRITE

The principles of pulsed field gradient (PFG) techniques[28] are beyond the scope of this article, and we provide only a brief description of the methods used in this study. In the proposed method the 2-D porosity maps are measured with centric-scan SPRITE,[13] a nonslice selective imaging technique.

The reciprocal-space formalism central to MRI introduces the spatial frequency vector $\boldsymbol{k} = \gamma \cdot G \cdot t_P \cdot (2 \cdot \pi)^{-1}$, where γ is the gyromagnetic ratio of the observed nuclei, G is the stepped gradient values, and t_P is the encoding time. The vector $\boldsymbol{k}$ forms a pair of Fourier conjugate variables with the physical space coordinate $\boldsymbol{r}$

$$S(k) = \int I(r) \cdot \exp(i \cdot 2 \cdot \pi \cdot k \cdot r) dr, \tag{6}$$

where $I(\boldsymbol{r})$ is a function proportional to the nuclear spin density $\rho_o(\boldsymbol{r})$. Sampling of k-space commences at its origin and proceeds to its extremities through a chosen trajectory. For each gradient step a nonselective radio frequency (RF) pulse is applied and a number of points of the free induction decay (FID) are acquired. Acquisition of multiple FID points can be performed to achieve an improved signal-to-noise ratio without an increase in experiment time.[29]

The RF pulse should be short enough to excite the maximum sample bandwidth $w = \gamma \cdot g_{\max} \cdot L \cdot (2 \cdot \pi)^{-1}$, where $g_{\max}$ is the maximum gradient strength, and L is the sample dimension along the gradient direction.

The delay between RF pulses (TR) is commonly less than the spin-lattice relaxation time constant T_1. This results in

image blurring due to partial saturation of longitudinal magnetization.[13,29] The use of low RF pulse flip angles, $\alpha \ll \pi/2$, in SPRITE substantially reduces the extent of the image blurring. The resolution achieved in typical centric-scan SPRITE measurements is within 0.5 to 1 mm range.

The SPRITE technique is designed to work with sample relaxation times as short as tens of microseconds. At the k-space origin the transverse magnetization is subject to exponential decay with an effective time constant T_2^*. The image intensity observed in centric-scan SPRITE is

$$I(r) = M(r) \cdot \exp(-t_P/T_2{}^*) \cdot \sin(\alpha), \tag{7}$$

where M is the local sample magnetization proportional to the local spin density, $\rho_o(\boldsymbol{r})$. The signal-to-noise ratio of the measurement depends essentially on the applied magnetic field and encoding time t_P. The encoding time is hardware limited and cannot be reduced below a certain value, defined by the maximum available gradient strength, field of view and probe ring-down time.

The single exponential FID allows simple quantitative porosity imaging in sedimentary rocks and concretes.[30] The single exponential FID is very typical for sedimentary rocks and concrete samples. However, in heterogeneous core samples containing domains with different rock fabric the T_2^* distribution may be quite noticeable. In such cases we will assume a single exponential decay within the same fabric domain.

Error in the MRI porosity measurement is proportional to the fraction of spins with $T_2^* \ll t_P$. A porosity map free of T_2^* weighting can be reconstructed from a series of centric-scan SPRITE images acquired with different t_P. Fitting these images to Eq. 7 will be a good approximation for sedimentary rocks and concretes. In a case when T_2^* weighting is critical, T_2^* may be controlled by the choice of an appropriate static magnetic field.

Fluid Velocity Measurements

Pulse scheme

A review article by Alley[31] encompasses recent achievements in magnetic resonance velocimetry. The pulse scheme used for 2-D flow visualization is shown in Figure 1. The displacement encoding is performed with the 13-interval APGSTE pulse sequence.[10] The stimulated echo pulse sequence is commonly employed to probe slow processes in systems with short spin-spin relaxation times T_2. The dynamic process takes place during the z-storage interval Δ_z, free of spin-spin relaxation. During this interval the spin system is subject to relatively slow spin-lattice relaxation only (T_1).

Two pairs of gradient pulses (duration $\delta/2$) encode the displacement of spins along the direction of the gradients. Phase encoding is achieved by incrementing these gradient in a number of steps N_q, from $-g_{\max}$ to $g_{\max}$. The phase and amplitude of the measured echo signal is sensitive to accumulated displacement of spins over time the interval $\Delta = \Delta_z + 3\tau/2 - \delta/12$.

This PFG scheme is designed to eliminate the cross-term between the background g_o, and applied gradients g, on condition $\delta_1 = \delta_2$. The term containing $g_o{}^2$ is substantially reduced as compared to the conventional stimulated echo sequence.

The longitudinal eddy-current delay (LED) allows the transient eddy-current fields to decay, thus, avoiding potential phase errors. The "spoil" gradients eliminate the residual transverse magnetization during the z-storage intervals. The centric-scan SPRITE part of the sequence introduces spatial encoding to the echo signal. The phase cycle of radio-frequency pulses is described elsewhere.[9]

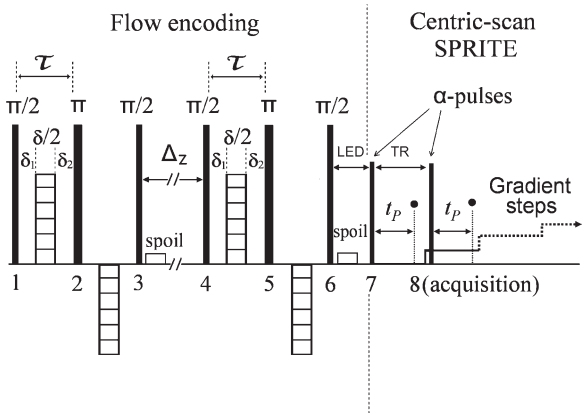

Figure 1. Alternating-pulsed-gradient stimulated-echo sequence (APGSTE) combined with centric-scan SPRITE.

The velocity imaging pulse sequence consists of the radio-frequency pulses (π, $\pi/2$ and α- flip angles) and pulsed-field gradients (encode times - $\delta/2$ and t_P).

Velocity distribution function

The displacement wavelength vector is defined as $\boldsymbol{q} = \gamma \cdot \delta \cdot \boldsymbol{g} \cdot (2 \cdot \pi)^{-1}$, where δ is the effective duration of the pulsed gradients. The wavelength vector $\boldsymbol{q}$, and the displacement vector $\boldsymbol{Z}$, form a pair of Fourier conjugate variables

$$S(q) = \int P_\Delta(Z) \cdot \exp(i \cdot 2 \cdot \pi \cdot q \cdot Z) dZ \tag{8}$$

$P_\Delta(\boldsymbol{Z}, \boldsymbol{r})$ is a probability distribution function of fluid displacement $\boldsymbol{Z}$, at observation time Δ. It describes the fluid displacement statistics covering all forms of translational molecular motion.[28]

The initial data set $S(\boldsymbol{q}, \boldsymbol{k})$, Fourier transformed along the k-space dimensions is given by

$$S(q,r) = \rho(r) \int P_\Delta(Z,r) \cdot \exp(i \cdot 2 \cdot \pi \cdot q \cdot Z) dZ, \tag{9}$$

where $\rho(r)$ is a function proportional to spatial distribution of the spin density. In terms of fluid velocity $\boldsymbol{V}$, Eq. 9 becomes

$$S(q,r) = \rho(r) \int P_\Delta(V,r) \cdot \exp(i \cdot 2 \cdot \pi \cdot q' \cdot V) dV, \tag{10}$$

where $q' = q \cdot \Delta$. Fourier transformation of Eq. 10 gives

$$P_\Delta(V,r) = \frac{\int S(q',r) \cdot \exp(-i \cdot 2 \cdot \pi \cdot q' \cdot V) dq'}{\rho(r)} \tag{11}$$

Parameters of the velocity distribution can be used for quantitative visualization of flow. A velocity value corresponding to the maximum probability V_{pk}, represents the largest fraction of molecules moving at the same velocity. This parameter does not adequately represent the total flow field and, therefore, works well only for flow systems and

experimental conditions with narrow and symmetric velocity distributions. In porous media like sedimentary rocks V_{pk} would typically correspond to stagnant or slowly moving fraction of the fluid. In sedimentary rocks the breadth of the velocity distribution is much greater than the spatial variation in the stagnant peak position.

Alternatively, the velocity map representation may be based on the ensemble-averaged velocity and variance of the velocity distribution $<V>$ and σ^2, respectively

$$<V>(r) = \int V \cdot P_{\Delta}(V,r)dV \tag{12}$$

$$\sigma^2(r) = \int (V - <V>(r))^2 \cdot P_{\Delta}(V,r)dV \tag{13}$$

The propagator should be corrected for a noise-induced offset that causes systematic underestimation of mean velocity with Eq. 12.

According to the Nyquist theorem the sampling rate should be high enough to ensure that $FOF/2$ is greater than the highest velocity in the flow. Components of the propagator expanding beyond the field of flow (FOF) encounter a ''folding'' about $\pm FOF/2$ and alter the true velocity distribution.

The mean velocity could be calculated accurately using echo values near the origin of q-space, thus, avoiding problems related to Eq. 12. The APGSTE signal can be expressed as follows

$$S(q') = \exp(i \cdot \varphi) \cdot \sum A_k \cdot \exp(2 \cdot \pi \cdot i \cdot V_k \cdot q') \cdot \exp(-f_k(q')), \tag{14}$$

where ϕ is the phase of the echo signal at $q' = 0$; A_k are weight coefficients representing probabilities of the velocity values V_k; and $f_k(q')$ is a set of real functions describing self-diffusion and random flow field dispersion mechanisms.[28] At $q' = 0$ one obtains

$$S(0) = \exp(i \cdot \varphi) \cdot \sum A_k \cdot \exp(-{f_k}^{q' \approx 0}) \tag{15}$$

The echo derivative at low q' limit ($q' \approx 0$) could be written as

$$\exp(-i \cdot \varphi) \cdot \frac{dS}{dq'}^{q' \approx 0} = \sum A_k \cdot \left(2 \cdot \pi \cdot i \cdot V_k \cdot \exp(-{f_k}^{q' \approx 0}) - \exp(-{f_k}^{q' \approx 0}) \frac{df_k}{dq'}^{q' \approx 0} \right) \tag{16}$$

Selecting the imaginary part (Im) of Eq. 16 one obtains

$$\mathrm{Im}\left(\exp(-i \cdot \varphi) \cdot \frac{dS}{dq'}^{q' \approx 0} \right) = 2 \cdot \pi \sum A_k \cdot V_k \cdot \exp(-{f_k}^{q' \approx 0}) \tag{17}$$

$$<V>(r) = \frac{\sum A_k V_k}{\sum A_k} \tag{18}$$

Assuming the dispersion factor $\exp(-f_k^{q' \approx 0})$ is reasonably close to 1 and combining Eqs. 15, 17 and 18 leads to

$$<V> = \frac{\mathrm{Im}\left(\exp(-i \cdot \varphi) \cdot \frac{dS}{dq'}^{q' \approx 0} \right)}{2\pi \cdot |S(0)|} \tag{19a}$$

Quantification of velocity distribution moments is addressed by Dyverfeldt et al.[32]

Eq. 19a is identical to a phase unwrapping approach

$$<V> = \frac{1}{2\pi} \frac{d}{dq'} \left(arctg \left(\frac{\mathrm{Im}(S \cdot \exp(-i \cdot \varphi))}{\mathrm{Re}(S \cdot \exp(-i \cdot \varphi))} \right) \right)^{q' \approx 0} \tag{19b}$$

Limitations

The choice of experimental parameters and conditions (δ, Δ, $g_{\max}$, flow rate) is crucial for quantitative velocity mapping. Attenuation of the stimulated echo due to relaxation and dispersion processes, taking place during τ and z-storage intervals, is given by

$$f = f_{\mathrm{relax}} \cdot f_D, \tag{20}$$

where

$$f_{\mathrm{relax}} = \exp(-4 \cdot \tau / T_2) \cdot \exp(-(\Delta_z + LED)/T_1), \tag{21}$$

$$f_D = \exp(-4\pi^2 \cdot q^2 \cdot D_{eff} \cdot C(\Delta, \tau, \delta), \tag{22}$$

where $D;_{eff}$ is an effective dispersion coefficient, and $C(\Delta,\tau, \delta) \approx \Delta$.

Expressions 21 and 22 define the range of applicability of the method. To avoid T_2, T_1 and diffusion weighting of the measured signal the parameters of the pulse sequence should satisfy the following requirements, respectively

$$4 \cdot \tau << T_2, \tag{23}$$

$$\Delta_z + LED << T_1, \tag{24}$$

and

$$\gamma^2 \cdot \delta^2 \cdot g_{\max}^2 \cdot \Delta << 1/D_{eff}, \tag{25}$$

As one can see from Eq. 21 the uncertainty of the velocity measurement will increase with the fraction of spins with $T_2 \ll 4 \cdot \tau$, and $T_1 \ll \Delta_z$ + LED. Bulk CPMG and inversion recovery measurements along with inverse Laplace transform will provide estimates of the lost fractions of magnetization.

A wide range of spin-spin relaxation times (T_2) related to the pore-size distribution is very common for fluids saturating sedimentary rocks.[33] The T_2 distributions in core plugs have a lower T_2 limit typically on the order of 1 ms that is comparable to the duration of the encoding intervals, τ.[34] The observation time Δ_z, is limited by the longitudinal relaxation time constant T_1. The T_1 values in sedimentary rocks fall in the range of tens to few hundred milliseconds. Effects of relaxation, dispersion and internal field inhomogeneity can shift the spectral weight of propagators.[23,24] The choice of short τ and Δ_z values should partially eliminate the relaxation and susceptibility related errors. The lower limit of the gradient pulse duration, $\delta/2$, is typically on the order of a hundred microseconds.

The dispersion coefficients in sedimentary rocks and unconsolidated porous media increase with the Peclet number.[35,36] High-dispersion coefficients within the core can

Table 1. Experimental Parameters

Sample	δ (*ms*)	Δ (*ms*)	g_{max} (*T/m*)	N_q	*L* (*cm*)	*D* (*cm*)	*Q* (*ml/min*)	Π (*kPa*) *at 24 °C*
PC/Bnth	0.8	17.3	0.019	3	4.9	2.41	8/7.6[†]	11.7
Corncockle	0.4	11	0.073	3	4.04	3.35	8/8.8[†]	64.8
Locharbriggs	1.64	18.6	0.032	4	5.3	3.8	8/9.1[†]	3
Spynie	0.8	17.6	0.037	3	5.02	3.79	8/8.4[†]	10.5
Fault	0.8	31.3	0.018	4	4.7	3.76	15/13[†]	27.6

[†]–The volumetric flow rate obtained by MRI.

cause displacements exceeding the pixel size. This results in a blurred velocity image. In the case of 3-D velocity imaging longitudinal and transverse dispersion coefficients should be taken into account. The transverse dispersion coefficient D_T, is typically smaller than the longitudinal coefficient D_L, by a factor ranging from 5 to 7.[35] For a given flow rate the observation interval Δ_z, should be chosen to minimize the loss of image resolution.

PFG techniques are well suited for studies of diffusion and dispersion processes in porous media.[28] Analytic expressions for diffusion attenuation in APGSTE experiments have been provided by Cotts et al.[10] For the 13-interval pulse sequence with condition I ($\delta_1 = \delta_2$) the echo attenuation due to diffusion is given by

$$ln(|S(q)|/|S(0)|) = -4\pi^2 \cdot q^2 \cdot D_{eff} \cdot (\Delta + 3\tau/2 - \delta/12) - \gamma^2 \cdot D_{eff} \cdot \tau^3 \cdot g_o^2 \cdot 4/3 \qquad (26)$$

The term containing ${g_0}^2$ does not depend on q, but can cause significant signal attenuation. In sandstones the background gradients are frequently larger than in limestones by some orders of magnitude.[37] The largest effective gradients are expected for pores with structure on a length scale of a few micrometers.

The primary goal of this study is a spatially resolved permeability measurement in the transverse plane of the cylindrical core. It assumes the measurement of mean axial velocity. As one can see from Eq. 19 full q-space sampling is not required, as all velocity distribution components contribute to the echo at the q-space origin. The accuracy of an approach based on Eq. 19 depends on the quality of q-space sampling. Acquiring a few echo points near the q-space origin with sufficient accuracy makes it a time efficient measurement. Data sampling over symmetric q-space range (from $-q_{max}$ to q_{max}) is SNR wise.

Geometric imperfections of the core holder and of the parts of the imaging system may result in misalignment of the core axis and the direction of the flow encoding gradient. It is a potential source of error in PFG velocity measurements. The transverse velocity components would contribute to the APGSTE signal, thus, contaminating the measurement of the axial flow components.

Experimental

MRI measurements

The MRI experiments were performed using a Tecmag (Houston, TX) Apollo console equipped with a Nalorac (Martinez, CA) 2.35 T 32 cm i.d. horizontal bore superconducting magnet. A water-cooled 7.5 cm i.d. gradient set driven by Techron (Elkhart, IN) 8710 amplifiers provided a gradient strength up to 1 T/m. The RF probe was a 4.7 cm inner dia. eight rung quadrature birdcage resonator. It provided homogeneous excitation within a spot 5.5 cm long.

Two-dimensional imaging averaged over the third dimension was performed by centric-scan SPRITE with four spiral k-space trajectories. Three-dimensional imaging was performed by centric-scan SPRITE with 39 conical k-space trajectories.[13] The excitation flip angle (α) was $\pi/30$ (0.7 μs); The T_2^* mapping was performed with encoding times (t_P) in the range of 0.1 to 1 ms; the repetition time (TR) was in the range of 1–2 ms, depending on the encoding time. Typical maximum gradient strengths employed in centric-scan SPRITE imaging were in the range of 0.10–0.20 T/m. The signal-to-noise (SNR) improvement was achieved by averaging of 4–9 FID points acquired during the SPRITE sampling. A Chirp z-Transform algorithm[29] was implemented to scale the field of view. The same 2-D imaging scheme was used for read-out in velocity mapping experiments.

The mean flow velocity was measured with 13-interval APGSTE combined with centric-scan SPRITE. The parameters of the flow encoding PFG scheme (δ, Δ, maximum gradient amplitude g_{max}, and number of q-steps N_q) are listed in Table 1; $\delta_1 = \delta_2 = 0.15$ ms.

The 16-step phase cycle was used;[9] 16 to 128 signal averages were acquired depending on SNR. The measurement of one 2-D velocity map takes from 15 to 60 min. The measurement time varies depending on the number of q-steps, image resolution T_1, and number of signal averages.

Reconstruction and processing of porosity, T_2^*, velocity and permeability images were performed in Matlab environment. The bulk T_2^*, T_1 and T_2 relaxation time constants were determined with standard FID, inversion recovery and CPMG measurements, respectively.

Samples

Two semicylinders of Bentheimer (Bad Bentheim, Germany) and Pink Clashach (Clashach Quarry, Scotland) sandstones were glued together with marine epoxy resin to form a composite cylindrical sample 4.9 cm long, 2.41 cm diameter. A series of sandstone cores (Corncockle, Locharbriggs, Spynie and a sandstone core containing fragments of fault facies) have diameters in the range of 3.7–3.8 cm and lengths of 4–5.3 cm. The dimensions of the samples (L, D), bulk flow rates (Q) and corresponding pressure drops (Π) are listed in Table 1.

The bulk porosities and permeabilities of the sandstones (Table 2) were determined with independent gravimetric and steady-state flow measurements, respectively. Distilled water was used for MRI and steady-state permeability measurements. No permeability alteration due to possible presence of clay in these samples was observed.

The flow through core system consisted of two homemade PEEK end plugs and 0.32 cm outside diameter high-pressure

Table 2. Bulk Porosity (Ø), Absolute Permeability (K) and Approximate Relaxation Time Constants (T_1, T_2, and T_2^*) Estimated from Biexponential Fit of Experimental FID, CPMG and Inversion Recovery Curves

Sample	Ø	K (D)	$T_1(ms)$	T_2 (ms)	T_2^* (ms)
Bnth	0.24 (±0.01)	1.8 (±0.2)	370 (80%)	280 (50%)	1.6
			40 (20%)	63 (50%)	
PC	0.14 (±0.01)	0.5 (±0.1)	345 (73%)	192 (51%)	0.6
			66 (27%)	36 (49%)	
PC/Bnth	0.189	1.1 (±0.1)	–	–	–
Corncockle	0.21	0.085 (±0.005)	196 (68%)	10.5 (68%)	0.33
			33 (32%)	75 (32%)	
Locharbriggs	0.26	1.9 (±0.1)	373 (67%)	23 (58%)	0.52
			65 (33%)	158 (42%)	
Spynie	0.17	0.52 (±0.05)	686 (84%)	288 (55%)	0.79
			74 (16%)	50 (45%)	
Fault	0.19	0.35 (±0.05)	246 (71%)	18 (63%)	0.83
			50 (29%)	117 (37%)	

plastic tubing. The diameters of the end plugs were 2.54 and 3.81 cm to fit the standard core diameters. The end plugs are provided with an axial port for transporting fluid to and from the sample. Each end plug has radial and circular grooves for distributing fluid to its entire injection face, and for collecting the fluid from all parts of its outflow face. The contribution of the PEEK end plugs to ^{1}H MRI signal was negligible due to critically short T_2^* of the material.

The tubing was connected to the end plugs with high-pressure plastic Swagelok fittings. A core sample is put between two end plugs and placed into AFLAS sleeve of the corresponding internal diameter. The whole assembly is sealed with one or two layers of Teflon heat shrink tubing. This design allows working without confinement pressure in a pressure range of 100–400 kPa.

A high-pressure pump QX-6000-SS (Vindum Engineering, San Ramon, CA), was employed to provide a constant flow rate through the sandstone samples. Measurements of the bulk permeability were performed at flow rates from 1 to 15 mL/min. The total pressure drop was measured based on digital data output from the pump pressure transducers. The pressure drop over the core was calculated as a difference of pressures measured for empty and loaded core holder at the same constant flow rate.

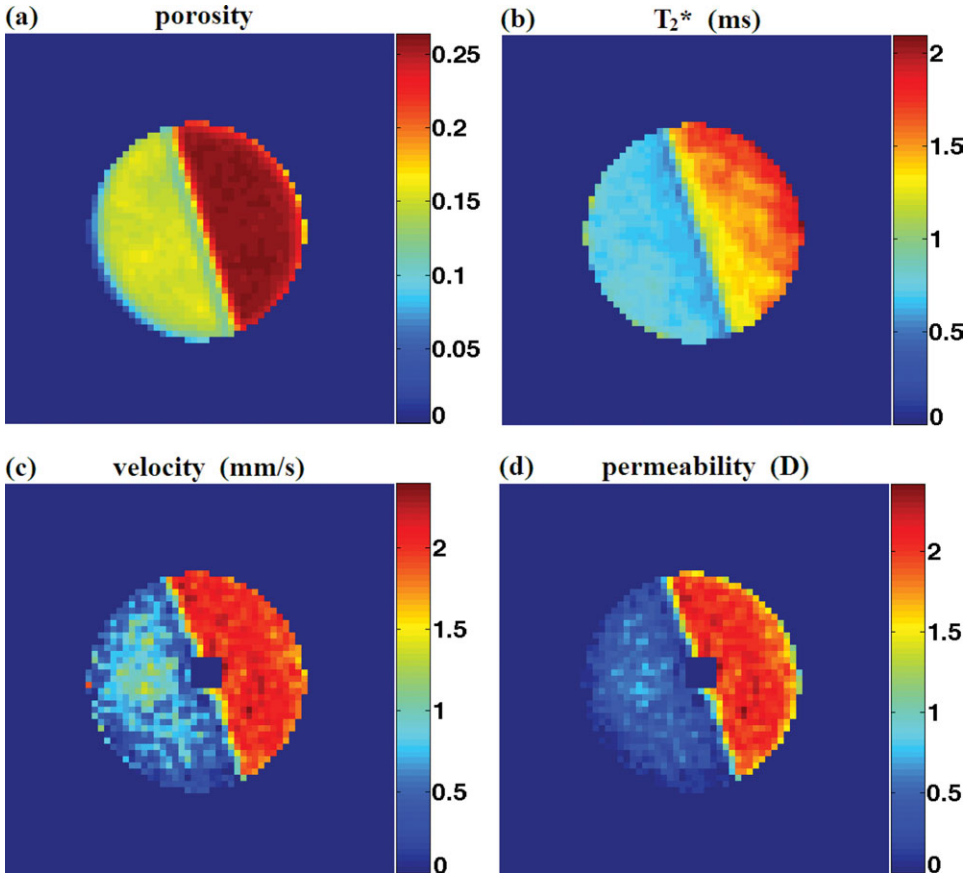

Figure 2. Water-saturated composite core PC/Bnth (Pink Clashach (left) and Bentheimer (right)).

(a) 2-D porosity map (x-y plane), (b) 2-D T_2^* map, (c) 2-D mean axial velocity map obtained for a volumetric flow rate of 8 mL/min (Reynolds numbers < 0.4), and (d) 2-D permeability map. FOV: 4.3 × 4.3 cm, 64 × 64. [Color figure can be viewed in the online issue, which is available at wileyonlinelibrary.com.]

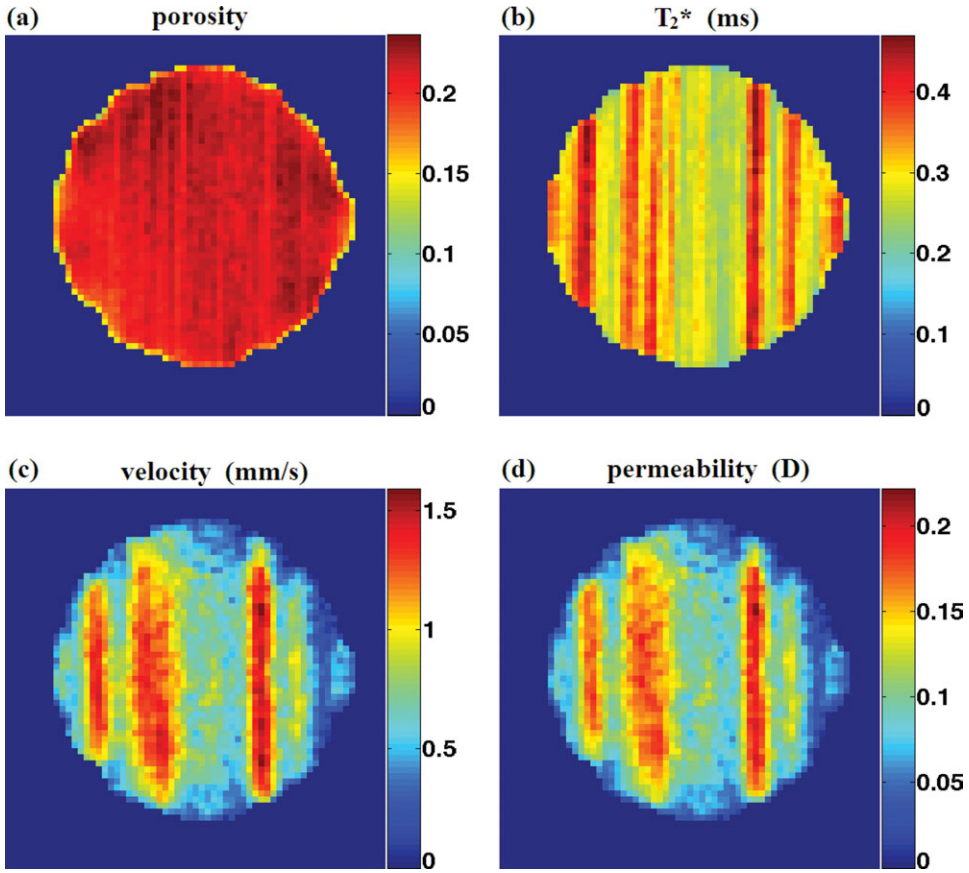

Figure 3. *Corncockle* sandstone.

(a) 2-D porosity map (*x*-*y* plane), (b) 2-D T_2^* map, (c) 2-D mean axial velocity map obtained for a volumetric flow rate of 8 mL/min (Reynolds numbers < 0.3), and (d) 2-D permeability map. FOV: 4.1 × 4.1 cm, 64 × 64. [Color figure can be viewed in the online issue, which is available at wileyonlinelibrary.com.]

Results and Discussion

The flow rates from 1 to 15 mL/min were established to be reasonable in terms of sensitivity and extent of dispersion in examined samples. In samples with bulk porosity from 15 to 25% these flow rates correspond to mean velocities from 0.05 to 1.5 mm/s. The lower flow rate limit is related to sensitivity of the PFG measurement. The duration of the flow-encoding gradient shouldn't significantly exceed the shortest T_2 of the rock. In addition to that the gradient amplitude is hardware limited. A significant number of signal averages is required to obtain satisfactory SNR in the accumulated phase at flow rates below 1 mL/min.

Transverse and longitudinal dispersion coefficients were obtained from the low-q limit of the magnitude echo decays using Eq. 26. For a flow rate of 8 mL/min and observation time of 16 ms these coefficients fall in the range of $2{\cdot}10^{-9}$ to $8{\cdot}10^{-8}$ m^2/s. This range is in good agreement with the literature data.[35] Within the observation time of 16 ms transverse dispersion causes spin displacements less than 60 μm. The longitudinal dispersion does not affect the 2-D axial velocity image in the transverse plane, since velocities are averaged along the core. At increasing flow rates the dispersion can approach the scale of resolution in the transverse plane. The fraction of fluid spreading beyond the pixel limits within a Δ interval can be estimated based on the measured dispersion coefficients. For a square pixel $a \times a$ in size this fraction is l/a, where l is the dispersion scale proportional to $(D_T \cdot \Delta)^{1/2}$. For the measured dispersion coefficients and a pixel of 1 × 1 mm^2 in size the fraction of fluid undergoing exchange between the neighboring pixels is less than 6%. Based on these estimations a velocity image resolution of 1 mm is fairly realistic.

The linear least square fitting of data in the low-q limit is the simplest approach for mean velocity calculation with Eqs. 19. The use of Eq. 19a is justified in the case when the dispersion factors in Eqs. 15 and 17 are reasonably close to 1. The effective dispersion on the timescale of Δ defines the range of q-space where the linear term of $\mathrm{Im}(S(q))$ dominates.[28]

In our case the observation time and mean velocities correspond to fluid displacements on a scale smaller than the sandstone grains (100–300 μm). This is a regime of preasymptotic dispersion, that is, the mean molecular displacement does not exceed the largest length scale of the flow-field heterogeneity. The range of q-space where $\mathrm{Im}(S(q'))$, and the phase of the signal $S(q')$ are essentially linear was estimated from high-sensitivity bulk measurements. The choice of q' values below 20 s/m would make the dispersion terms $f_k(q') < 0.1$ and the exponential factors $\exp(-f_k^{q'\approx 0}) > 0.9$. For an ensemble of molecules moving at a velocity V_k the phase of the APGSTE signal, $S(q')$, is $2{\cdot}\pi{\cdot}V_k{\cdot}q'$. The phase low enough to ensure that $\mathrm{Im}(S(q')) \approx 2{\cdot}\pi{\cdot}V_k{\cdot}q'$ will allow linear fitting of the APGSTE signal. For phases $x < \pi/6$, $|x-\sin(x)|/x < 0.045$, i.e., error does not exceed 4.5%. The q-range and mean flow velocities considered in this study

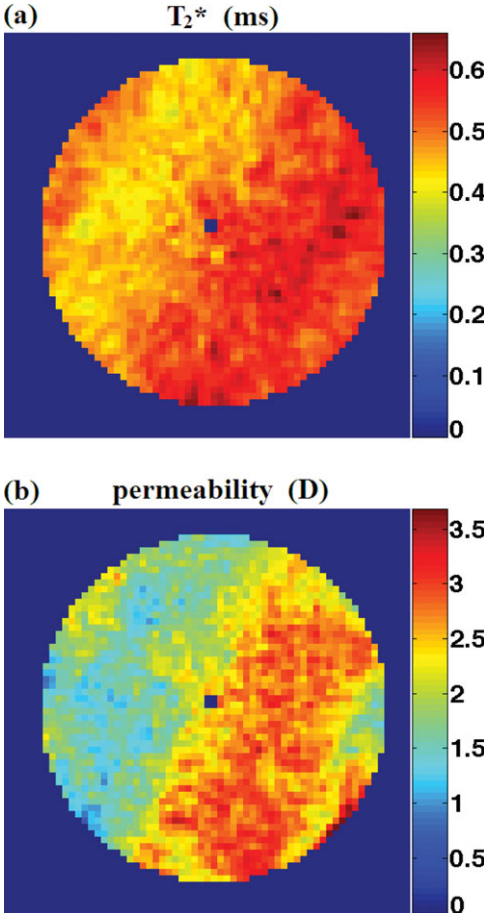

Figure 4. *Locharbriggs* sandstone.

(a) 2-D T_2^* map, and (b) 2-D permeability map; the corresponding velocity map was obtained for a volumetric flow rate of 8 mL/min (Reynolds numbers < 0.2). FOV: 4.1 × 4.1 cm, 64 × 64. [Color figure can be viewed in the online issue, which is available at wileyonlinelibrary.com.]

correspond to a phase span of $0–2\cdot\pi/25$. The parameters of the APGSTE pulse sequence are given in Table 1.

Composite sandstone

The composite sandstone core (PC/Bnth) represents an artificial "parallel circuit" sample with two distinct permeability domains. The bulk porosities, permeabilities and relaxation time constants of the sandstones are listed in Table 2. 12 centric-scan SPRITE images across the composite core sample were acquired with different encoding times, t_P, and fitted to Eq. 7.

The resulting porosity map is free of T_2^* weighting, Figure 2a. The T_2^* map is displayed in Figure 2b. The porosity map agrees within 5% with the gravimetric porosities of Bentheimer and Pink Clashach cores (Table 2).

A mean axial velocity map obtained for volumetric flow rate of 8 mL/min is displayed in Figure 2c. The volumetric flow rates calculated based on porosity and mean velocity images are provided in Table 1. The permeability map reconstructed with the porosity and velocity maps is shown in Figure 2d. The constant factors used in Eq. 5 are listed in Table 1. The permeability values agree with the bulk values within 10% difference. The central regions of the velocity and permeability maps are masked as they overlap with the velocity spikes from fluid inside inflow/outflow tubing.

Corncockle sandstone

The *Corncockle* sample is a pale red, noncalcareous, fine to medium grained sandstone extracted from Corncockle Quarry, Scotland. The bedding layers are hardly distinguishable by eye. The bulk FID could be roughly represented by an effective time constant around 0.33 ms (Table 2). A number of 2-D centric-scan SPRITE images were obtained with encoding times in the range of 0.1 to 1 ms. They were used to reconstruct porosity and T_2^* maps, displayed in Figure 3a and b, respectively. The spatially resolved FIDs were fairly monoexponential. However, narrow T_2^* distributions within image pixels were possible. The layered texture of the sample is clearly visible in the T_2^* and porosity images. The porosity variation across the layers is close to 20% of the bulk porosity. The bedding planes are distinguished even better through the T_2^* contrast, Figure 3b.

Significant contrast was also observed in the mean axial velocity map, Figure 3c. With the given number of factors affecting the velocity measurement, the observed velocity contrast may be questioned. Particular attention should be paid to transverse relaxation and echo attenuation due to internal gradients within τ intervals. A combination of these processes can influence the measured velocity image. A number of different lines of evidence, however, suggest that

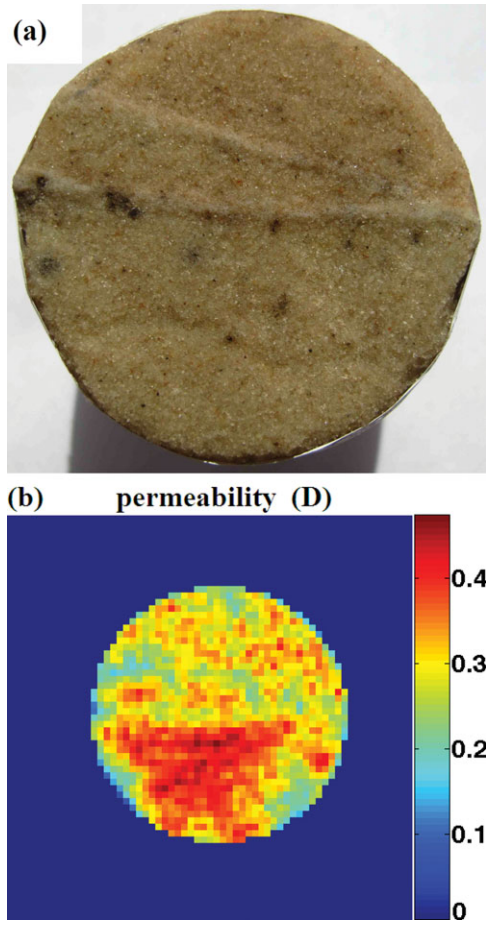

Figure 5. Fault sandstone.

(a) A photograph of the fault sandstone core, and (b) 2-D permeability map; the corresponding 2-D velocity map was obtained for a volumetric flow rate of 15 mL/min (Reynolds numbers < 0.3). FOV: 5.5 × 5.5 cm, 64 × 64. [Color figure can be viewed in the online issue, which is available at wileyonlinelibrary.com.]

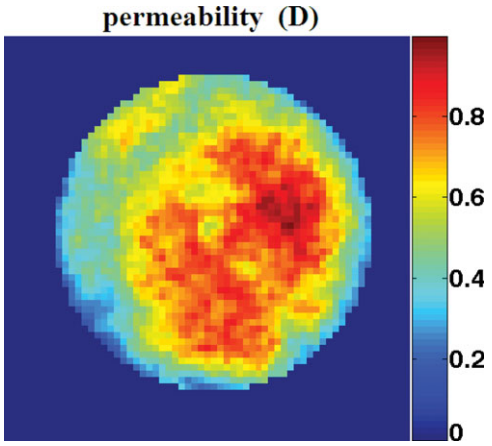

Figure 6. *Spynie* sandstone.

2-D permeability map obtained for a volumetric flow rate of 8 mL/min (Reynolds numbers < 0.2). FOV: 4.3 × 4.3 cm, 64 × 64. [Color figure can be viewed in the online issue, which is available at wileyonlinelibrary.com.]

the observed velocity contrast is correct. The first and most basic criterion is the good correspondence of velocity maps with the bulk flow rate (10% difference).

Measured velocities can deviate from the true mean values due to T_2-weghting within the encoding intervals τ. The fraction of magnetization with $T_2 < 4{\cdot}\tau$ was estimated from inverse Laplace transformation of the bulk CPMG decay. This fraction is close 25% at 2.4 T, with the "cut-off" point of T_2 distributions around 1.2 ms. The lost magnetization corresponds to fluid occupying the smallest pores. In fine to medium grained sandstones a volume on the order of tens of grains contains a broad spectrum of pore sizes. In our case the pixel in the transverse plane (0.64 × 0.64 mm^2) is large compared to the sandstone grains. The water mobility in smaller pores is relatively more restricted and, therefore, T_2 -weighting should cause some overestimation of mean velocity in every pixel of the 2-D image. Due to the macroscopic heterogeneity of the core sample, the T_2 distributions within individual pixels are expected to be narrower than the bulk distribution. Therefore, the T_2 weighting affects the velocity distribution within each pixel in a more uniform way as compared to that effect on the bulk velocity distribution.

The effects of internal gradients on the velocity measurement are expected to increase with the flow rate. As spins move slow enough to remain within the same background gradient during the observation interval the measured velocity should approach the true mean value. Effects from T_2-weighting and background gradients may compensate one another resulting in an expected mean velocity value. This situation is possible since T_2-weighting and background gradients affect fast and slow moving spins in a different way. Slow moving spins are more suppressed by T_2-relaxation than by background gradients. The inverse situation is expected for fast moving spins. Since the dependences of these effects on τ are different (Eqs. 21 and 26) the velocity contrast should change with τ. The velocity contrast displayed in Figure 3c, however, was observed for a range of flow rates from 1 to 12 mL/min and a range of τ from 0.7 to 1.5 ms.

A permeability map calculated with Eq. 5 is displayed in Figure 3d. It clearly indicates presence of parallel lamination in the core. Layered variation in composition, porosity and permeability in sedimentary rocks is very common. The genesis and types of laminations are well addressed in the literature.[38,39]

Locharbriggs sandstone

The *Locharbriggs* sample is a red-pink medium grained sandstone from the Locharbriggs Quarry in Dumfries, Scotland. This sandstone is one order of magnitude more permeable than Corncockle (Table 2). The bulk FID is dominated by the T_2^* time constant of 0.52 ±0.1 ms. The T_2^* contrast displayed in Figure 4a is indicative of a layered core structure.

The relaxation time constants are remarkably longer than in the Corncockle sandstone that makes the Locharbriggs core a lesser challenge for APGSTE-SPRITE measurement.

The porosity contrast is hardly noticeable (not shown).

The revealed permeability contrast is mainly due to the mean velocity contrast, Figure 4b. The apparent range of permeability in the *Locharbriggs* sample is from 0.5 to 3.5 D.

Fault sandstone

A fault is defined as a displacement of rock layers resulting in a modification of petrophysical properties in a volume of rock. Faults are included in most petroleum reservoirs and

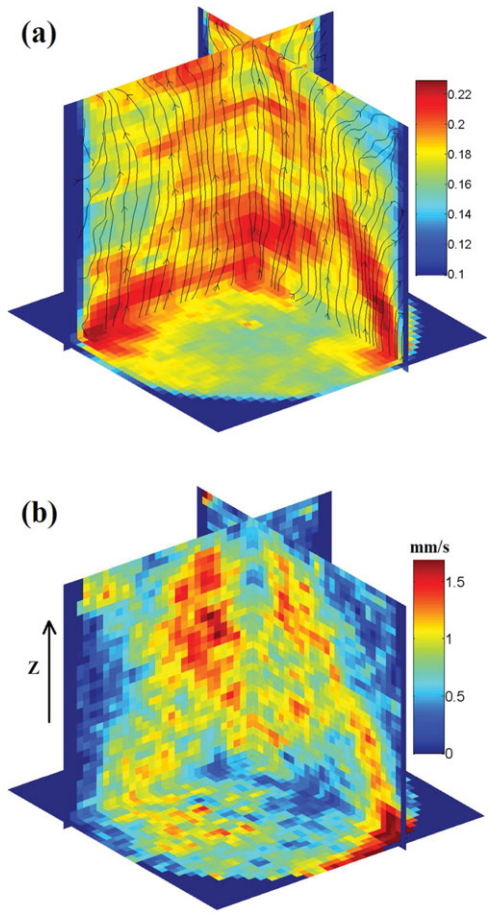

Figure 7. *Spynie* sandstone.

(a) Longitudinal and transverse slices of the 3-D porosity map and projections of streamlines reconstructed from the full 3-D velocity field, and (b) slices of the 3-D axial velocity map (3 *q*-space points). [Color figure can be viewed in the online issue, which is available at wileyonlinelibrary.com.]

have complicated 3-D geometries. Faults are known to restrict fluid flow due to low-permeability characteristics.

The fragments of a fault zone are visible in a photograph of the sandstone core sample, Figure 5a. The two parts of the core across the central fault line are slightly different in color indicating differences in composition and structure. The permeability map is displayed in Figure 5b. Although the fault planes are not perfectly aligned with the core axis, they are clearly distinguished in the permeability map. Higher permeability of the lower half of the core is apparent.

Spynie sandstone

The *Spynie* sample is a pale yellow buff, calcareous, fine grained sandstone from Spynie Quarry, Scotland. It has no obvious bedding planes. The bulk FID was clearly monoexponential. The product of 2-D porosity and velocity maps resulted in 2-D permeability displayed in Figure 6.

Porosity variation within the core was distinguished by 3-D centric-scan SPRITE imaging, Figure 7a. The visible heterogeneities are on the order of 0.5 to 2 cm in size. Low-porosity-permeability domains randomly localized within the core volume create zones of obstructed flow. Averaging of permeability along the core caused the observed contrast in 2-D permeability map.

For systems with random bulk texture, 3-D imaging of mean velocity projections can provide detailed information on the heterogeneity of the flow field. A full velocity field can be obtained with APGSTE-conical SPRITE method within 4 h by sampling three q-space points in each spatial direction. Longitudinal and transverse slices of the 3-D axial velocity map are displayed in Figure 7b. The transverse slices agree with the actual volumetric flow rate within 10% difference. 3-D streamlines reconstructed using the full velocity field data indicate that the fluid tends to bypass the domains with lower porosity, that is, the flow tends to occur in high permeability domains. The projections of the streamlines on axial slices of the 3-D porosity map are shown in Figure 7a.

Conclusions

The proposed permeability mapping technique is advantageous for the characterization of fluid flow in a wide variety of porous and granular media with strong internal magnetic field gradients. The method is based on quantitative porosity and velocity imaging with centric-scan SPRITE and APGSTE prepared centric-scan SPRITE, respectively. The method was tested on heterogeneous sandstone cores with bulk permeabilities from 85 to 1900 mD. The 2-D permeability maps showed excellent agreement with conventional steady-state flow measurements. The method allows accurate predictions of the capacity of large-scale petroleum reservoirs.

The influence of the internal gradients on velocity measurements can be controlled (to some extent) through the choice of the static magnetic field strength. A high-pressure core holder will be required for flow studies in low-permeability cores. The method is well suited for characterization of multiphase flow systems and relative permeability measurements.

The time-efficiency of velocity measurements is increased through echo sampling near the q-space origin. This approach is suited for 3-D mapping of mean velocity vectors in petroleum reservoir cores. 3-D velocity and porosity maps will provide a valuable basis for numerical modeling of flow in porous media.

Acknowledgments

BJB thanks NSERC for Discovery grant. Petroleum Research Atlantic Canada is thanked for financial support, as is the Canada Chairs program for a Research Chair in MRI of Materials. The authors thank Prof. Christopher Hall and Dr. Geir Ersland for the provided sandstone samples.

Literature Cited

1. Kenyon WE. Petrophysical principles of applications of NMR logging. *Log Analyst*. 1997;38:21–43.
2. Coates GR, Xiao L, Prammer MG. *NMR Logging Principles and Applications*. Houston, TX: Halliburton Energy Services Publications; 1999.
3. Guilfoyle DN, Mansfield P. Fluid flow measurement in porous media by echo-planar imaging. *J Magn Reson*. 1992;97:342–358.
4. Mansfield P, Issa B. Fluid Transport in porous rocks. I. EPI Studies and a stochastic model of flow. *J Magn Reson Ser A*. 1996;122:137–148.
5. Chang CTP, Watson AT. NMR Imaging of flow velocity in porous media. *AIChE J*. 1999;45(3):437–444.
6. Klemm A, Kimmich R, Weber M. Flow through percolation clusters: NMR velocity mapping and numerical simulation study. *Phys Rev E*. 2001;63:041514–1—041514–8.
7. Weber M, Kimmich R. Maps of electric current density and hydrodynamic flow in porous media: NMR experiments and numerical simulations. *Phys Rev E*. 2002;66:026306–1—026306–9.
8. Bencsik M, Chandrasekhar R. Method for measuring local hydraulic permeability using magnetic resonance imaging. *Phys Rev E*. 2001;63:065302–1–065302–4.
9. Li L, Chen Q, Marble AE, Romero-Zeryn L, Newling B, Balcom BJ. Flow imaging of fluids in porous media by magnetization prepared centric-scan SPRITE. *J Magn Reson*. 2009;197:1–8.
10. Cotts RM, Hoch MJR, Sun T, Marker JT. Pulsed field gradient stimulated echo methods for improved NMR diffusion measurements in heterogeneous systems. *J Magn Reson*. 1989;83:252–266.
11. Gibbs SJ, Johnson Jr CS. A PFGNMR experiment for accurate diffusion and flow studies in the presence of eddy current. *J Magn Reson*. 1991;93:395–402.
12. Mastikhin IV, Mullally H, MacMillan B, Balcom BJ. Water content profiles with a 1D centric SPRITE acquisition. *Can J Chem*. 1998;76:1753–1765.
13. Halse M, Goodyear DJ, MacMillan MB, Szomolanyi P, Matheson D, Balcom BJ. Centric scan SPRITE magnetic resonance imaging. *J Magn Reson*. 2003;165:219–229.
14. Romanenko KV, Balcom BJ. Permeability mapping in porous media by magnetization prepared centric-scan SPRITE. *Experiments in fluids*. 2011;50(2):301–312.
15. Balcom BJ, MacGregor RP, Beyea SD, Green DP, Armstrong RL, Bremner TW. Single point ramped imaging with T_1 enhancement (SPRITE). *J Magn Reson Ser A*. 1996;123:131–134.
16. Beyea SD, Balcom BJ, Prado PJ, Cross AR, Kennedy CB, Armstrong RL, Bremner TW. Relaxation time mapping of short T_2^* nuclei with single-point imaging (SPI) methods. *J Magn Reson*. 1998;135:156–164.
17. Prado PJ, Balcom BJ, Mastikhin IV, Cross AR, Armstrong RL, Logan A. Magnetic resonance imaging of gases: a single-point ramped imaging with T1 enhancement (SPRITE) study. *J Magn Reson*. 1999;137:324–332.
18. Li L, Marica F, Chen Q, MacMillan B, Balcom BJ. Quantitative discrimination of water and hydrocarbons in porous media by magnetization prepared centric-scan SPRITE. *J Magn Reson*. 2007;186:282–292.
19. Romanenko KV, Cano-Barrita PF, Bruce BJ. ^{35}Cl profiling using centric scan SPRITE with variable flip angle excitation. *J Magn Reson*. 2009;198:24–30.
20. Karger J, Heink W. The propagator representation of molecular transport in microporous crystallites. *J Magn Reson*. 1983;51:1–7.
21. Seymour JD, Callaghan PT. Generalized Approach to NMR Analysis of flow and dispersion in porous media. *AIChE J*. 1997;43:2096–1997.
22. Scheven UM, Verganelakis D, Harris R, Johns ML, Gladden LF. Quantitative nuclear magnetic resonance measurements of

preasymptotic dispersion in flow through porous media. *Phys Fluids*. 2005;17:117107–1–117107–7.
23. Mitchell J, Graf von der Schulenburg DA, Holland DJ, Fordham EJ, Johns ML, Gladden LF. Determining NMR flow propagator moments in porous rocks without the influence of relaxation. *J Magn Reson*. 2008;193:218–225.
24. Scheven UM, Seland JG, Cory DG. NMR-propagator measurements on flow through a random pack of porous glass beads and how they are affected by dispersion, relaxation and internal field inhomogeneities. *Phys Rev E*. 2004;69:021201–1–021201–9.
25. Chen S, Doolen GD. Lattice Boltzmann method for fluid flows. *Annu Rev Fluid Mech*. 1998;30:329–364.
26. Dandekar AY. *Petroleum Reservoir Rock and Fluid Properties*. CRC Press; 2006.
27. Gruesbeck C, Collins RE. Entrainment and deposition of fine particles in porous media. *Soc Pet Eng J*. 1982;22:847–856.
28. Callaghan PT. *Principles of Nuclear Magnetic Resonance Microscopy*. Oxford, UK: Clarendon Press; 1991.
29. Halse M, Rioux J, Romanzetti S, Kaffanke J, MacMillan B, Mastikhin I, Shah NJ, Aubanel E, Balcom BJ. Centric scan SPRITE magnetic resonance imaging: optimization of SNR, resolution, and relaxation time mapping. *J Magn Reson*. 2004;169:102–117.
30. Chen Q, Marble AE, Colpitts BG, Balcom BJ. The internal magnetic field distribution, and single exponential magnetic resonance free induction decay, in rocks. *J Magn Reson*. 2005;175:300–308.
31. Elkins CJ, Alley MT. Magnetic resonance velocimetry: applications of magnetic resonance imaging in the measurement of fluid motion. *Exp Fluids*. 2007;43:823–858.
32. Dyverfeldt P, Sigfridsson A, Knutsson H, Ebbers T. A novel MRI framework for the quantification of any moment of arbitrary velocity distributions. *Magn Reson Med*. 2011;65:725–731.
33. Hürlimann MD, Helmer KG, Latour LL, Sotak CH. Restricted diffusion in sedimentary rocks. Determination of surface-area-tovolume ratio and surface relaxivity. *J Magn Reson A*. 1994;111:169–178.
34. Kleinberg RL. *Nuclear magnetic resonance*. In: *Po-zen Wong*, ed. *Methods in the Physics of Porous Media*. San Diego; CA: Academic Press; 1999:337–377.
35. Bear J. *Dynamics of Fluids in Porous Media*. New York: Dover Publications; 1988:162–164.
36. Bijeljic B, Muggeridge AH, Blunt MJ. Pore-scale modeling of longitudinal dispersion. *Water Resources Res*. 2004;40:W11501.
37. Hürlimann MD. Effective gradients in porous media due to susceptibility differences. *J Magn Reson*. 1998;131:232–240.
38. Boggs Jr S. *Principles of Sedimentology and Stratigraphy*. Chicago, IL: Merrill Publishing Co; 1987.
39. Blatt H, Tracy RJ, Owens BE. *Petrology, Igneous, Sedimentary, and Metamorphic*. 3rd ed. New York, NY: W.H. Freeman & Co; 2006.

Manuscript received Oct. 17, 2011, revision received Dec. 20, 2011, and final revision received Feb. 14, 2012.